AGU PUBLICATIONS

[Geophysical Research Letters]

Supporting Information for

Revisiting Model – Observation Discrepancies in Recent Pacific SST Trends Using an Observational Large Ensemble

Sieu-Cuong San[1,2], Clara Deser[1*], Pedro DiNezio[2,3], Adam S. Phillips[1], Tongtong Xu[4,5], Robert C. J. Wills[6] and Karen A. McKinnon[7]

October 1, 2026

[1] Climate and Global Dynamics Laboratory, National Center for Atmospheric Research, Boulder, CO, USA.

[2] The ATLAS Institute, University of Colorado Boulder, Boulder, CO, USA.

[3] Departamento de Hidráulica, Facultad de Ciencias Exactas, Físicas y Naturales, Universidad Nacional de Córdoba, Córdoba, Argentina.

[4] CIRES, University of Colorado Boulder, Boulder CO, USA.

[5] NOAA Physical Sciences DivisionLaboratory, Boulder CO, USA.

[6] Institute for Atmospheric and Climate Science, ETH Zurich, Universitätstrasse 16, Zurich, Switzerland.

[7] Department of Atmospheric and Oceanic Sciences, Department of Statistics and Data Science, Institute of the Environment and Sustainability, University of California, Los Angeles.

* Corresponding author: Clara Deser (cdeser@ucar.edu)

Contents of this file

Texts S1 to S4

Figures S1 to S14

Introduction

The supporting information presented here provides additional details on the Linear Inverse Model (LIM) and its validation using the CESM2-LE as a perfect-model testbed, construction of the Observational Large Ensemble (OBS-LE), estimation of the observed forced response and internal variability, and trend metrics and statistical analyses. It also includes the supporting figures referenced in the main text.

Text S1. Linear Inverse Model and Construction of the OBS-LE

The linear inverse model (LIM) approximates the evolution of a climate anomaly state vector as a linear dynamical system driven by stochastic forcing (Hasselmann, 1988; Penland & Sardeshmukh, 1995):

$$\frac{\mathrm{d}\mathbf{x}}{\mathrm{d}t} = \mathbf{L}\mathbf{x} + \boldsymbol{\xi} \tag{1}$$

where **x**(t) is the climate state vector, **L** is the linear dynamical operator governing the deterministic evolution of the system, and $\boldsymbol{\xi}(t)$ represents white-noise stochastic forcing (with spatial coherence). This formulation assumes a separation between relatively slow, approximately linear climate dynamics and faster and nonlinear processes that can be represented statistically as stochastic forcing (Capotondi et al., 2022a; Zhao et al., 2021).

The linear operator **L** is estimated empirically from the lagged covariance statistics of the state vector:

$$\mathbf{L} = \tau^{-1} \ln[\mathbf{C}(\tau)\mathbf{C}(0)^{-1}] \tag{2}$$

where $\mathbf{C}(0) = \langle \mathbf{x}(t)\mathbf{x}^{\mathrm{T}}(t) \rangle$ and $\mathbf{C}(\tau) = \langle \mathbf{x}(t+\tau)\mathbf{x}^{\mathrm{T}}(t) \rangle$ denote the zero-lag and lag-τ covariance matrices, respectively. Here τ is the training lag. In this study, we use a lag of 3 months to estimate the LIM operator. For the resulting system to be dynamically stable, all eigenvalues of **L** must have negative real parts, corresponding to modes that decay

asymptotically with time. Because these modes need not be orthogonal, their interaction can produce transient growth over finite intervals, which can represent transient growth associated with phenomena such as ENSO.

Once $\mathbf{L}$ is known, the covariance of the stochastic forcing, $\mathbf{Q} = \langle \boldsymbol{\xi}(t)\boldsymbol{\xi}^{\mathrm{T}}(t) \rangle$, is constrained by requiring the system statistics to remain stationary – a balance condition known as the fluctuation–dissipation relation (Penland & Matrosova, 1994):

$$\mathbf{L}\mathbf{C}(0) + \mathbf{C}(0)\mathbf{L}^{\mathrm{T}} + \mathbf{Q} = 0 \tag{3}$$

State vector construction. We describe the climate state using monthly SST from the Extended Reconstructed SST Version 5 (ERSSTv5; Huang et al., 2017) and sea surface height (SSH) from the Ocean Reanalysis System 5 (ORAS5; Zuo et al., 2019) over the global domain from 70°S to 70°N, combining the two fields jointly to better represent coupled upper-ocean variability (Capotondi et al., 2022; Rebert et al., 1985; Zhang et al., 2024). We also tested a pan-Pacific domain (70°S–70°N, 120°E–70°W) and obtained similar results. Before constructing the LIM, we remove the mean seasonal cycle from the SST and SSH fields, and then remove their seasonally varying externally forced components as described in Text S2. We also apply a 3-month running mean to the residual anomalies to reduce high-frequency variability following Newman et al. (2011).

We perform separate empirical orthogonal function (EOF) analyses of the resulting internal SST and SSH anomalies over 70°S–70°N during 1960–2022 (our choice of start year is dictated by the availability of ORAS5 SSH). The LIM is constructed jointly in a reduced EOF space, retaining the leading 20 SST (ERSSTv5) PCs and 10 SSH (ORAS5) PCs, which explain 80% of the SST variance and 66% of the SSH variance. We also apply the same LIM methodology to each member of the 50-member CESM2-LE with smoothed biomass burning forcing (Rodgers et al. 2021). Across the 50 CESM2-LE members, the 20 retained SST EOFs explain approximately 84% of the variance (range: 82%–86%), while the 10 retained SSH EOFs explain approximately 70% (range: 66%–75%), comparable to that in observations.

Before combining the SST and SSH PCs into a single state vector, the PCs associated with each field are scaled by the square root of the sum of the retained eigenvalues for that field. This scaling prevents either SST or SSH from dominating the joint covariance structure solely because of differences in their overall variance. We also examined alternative combinations of SST/SSH PCs – 22/10, 18/10, 16/10, 22/12, 20/12, 18/12, 16/12, 22/14, 20/14, 18/14, 16/14, 22/16, 20/16, 18/16, and 16/16 – and obtained qualitatively similar results (not shown).

Numerical integration. Synthetic realizations are generated by integrating the stationary LIM forward in time with stochastic forcing. Following the two-step stochastic integration scheme of Penland & Matrosova (1994), an intermediate state is first advanced according to:

$$\mathbf{y}(t+\Delta t) = [\mathbf{I} + \mathbf{L}\Delta t]\mathbf{y}(t) + \sqrt{\Delta t}\,\mathbf{S}\mathbf{r}(t) \tag{4}$$

and then averaging the updated and previous intermediate states to obtain the state vector at the half time step:

$$\mathbf{x}\left(t + \frac{\Delta t}{2}\right) = \frac{\mathbf{y}(t+\Delta t) + \mathbf{y}(t)}{2} \tag{5}$$

Here, $\mathbf{I}$ is the identity matrix, $\Delta t = 16$ h is the integration time step (Xu et al., 2022), and $\mathbf{r}(t)$ is a vector of independent random draws from a standard Gaussian distribution with zero mean and unit variance. The stochastic forcing amplitude matrix is given by $\mathbf{S} = \mathbf{V}\boldsymbol{\Lambda}^{1/2}$, where $\mathbf{V}$ and $\boldsymbol{\Lambda}$ contain the eigenvectors and corresponding eigenvalues of the stochastic forcing covariance matrix $\mathbf{Q}$.

Generating the synthetic ensemble. After estimating the LIM operator $\mathbf{L}$ and stochastic forcing covariance $\mathbf{Q}$, we integrate the stochastic system forward continuously. The integration begins with a 2,000-year spin-up, which is discarded to minimize sensitivity to the initial condition. The subsequent integration is divided into nonoverlapping 42-year realizations corresponding to the length of the study period (1979–2020). Each realization

is transformed from the reduced EOF space back into physical space to produce a synthetic evolution of internally generated SST variability.

For the OBS-LE, we generate 50,000 synthetic internal-variability realizations constructed with the LIM and then add back in the forced SST evolution provided by the Forced Statistical Method Intercomparison Project (ForceSMIP; Wills et al. 2026). Thus, all OBS-LE members share the same estimated externally forced response but contain independent realizations of internal variability. The large ensemble size provides robust sampling of the internal-variability distribution, including its tails, which is important for the percentile-based comparisons presented in Section 3.

Text S2. Observed Forced Response and Internal Variability

The observed SST record contains contributions from both externally forced climate change and internal variability (see Figure S1 for the total, forced and internal components of ERSSTv5 linear trends computed over the period 1979–2020). For the forced component, we use a state-of-the-art estimate provided by ForceSMIP (Wills et al. 2026; we note that ERSSTv5 was the only SST dataset considered in ForceSMIP, dictating our choice for this study). We obtain the internal component by subtracting the ForceSMIP estimate from ERSSTv5 at each location and time. This internal component is used in the LIM for constructing the OBS-LE.

ForceSMIP includes a total of 30 statistical and machine learning methods, each of which was evaluated in a common framework based on model LEs, for which the forced response is known. Specifically, the skill of each method in isolating the forced response in single realizations of model LEs was assessed across a wide range of metrics including multi-decadal trends. The skillful methods were then applied to ERSSTv5, thereby providing estimates of the observed forced response. Here, we use the average across the 27 methods that were skillful for SST trends as our best estimate of observed forced response (see Fig. 11 in Wills et al. 2026).

Because an equivalent ForceSMIP estimate is not available for SSH, we estimate the forced SSH component from the SSH reconstruction associated with the least-damped mode (LDM) of the joint SST–SSH state (Alexander et al., 2022; Newman, 2013; Xu et al., 2022)

and define internal SSH as the residual after removing this component from ORAS5. The similarity between the LDM and ForceSMIP estimates of the forced component of ERSSTv5 (Figure S5) lends confidence to our use of the LDM for the forced component of SSH; however, this should be revisited in future studies once ForceSMIP estimates for SSH become available.

Text S3. Trend Metrics and Statistical Analysis

We focus on annual-mean SST trends over 1979–2020 to facilitate direct comparison with Wills et al. (2022). Repeating the analysis for 1980–2022 yields qualitatively similar results (note that the ForceSMIP data is not available past 2022). All trends are computed based on linear least-squares regression and shown as the change in SST (°C) over the analysis period.

We evaluate two regional metrics of tropical Pacific SST trends following the definitions in Wills et al. (2022): 1) the equatorial Pacific zonal SST gradient index, defined as the difference between SST averaged over the western equatorial Pacific (5°S–5°N, 110°E–180°) and the eastern equatorial Pacific (5°S–5°N, 180°–80°W); and 2) the Indo-Pacific Warm Pool (IPWP)-to-tropical-mean warming ratio, defined as the SST trend averaged over the IPWP (30°S–30°N, 50°E–160°W) divided by the SST trend averaged over the entire tropical domain (30°S–30°N).

We also evaluate the spatial agreement between simulated and observed SST trend patterns using area-weighted pattern correlation and root-mean-square error (RMSE). These metrics are calculated over the global (70°S–70°N), pan-Pacific (70°S–70°N, 120°E–70°W), and tropical Pacific (30°S–30°N, 120°E–70°W) domains. The domain-mean is removed before computing pattern correlations.

For visualization, probability density functions are estimated using kernel density estimation (KDE) with MATLAB's default Gaussian kernel and automatic bandwidth selection. Percentiles and percentile ranks are calculated empirically from the underlying samples rather than from the fitted KDEs.

Text S4. LIM validation and CESM2 Comparison

We first evaluate the LIM using the 50-member CESM2-LE with smoothed biomass burning (Rodgers et al. 2021) as a perfect-model testbed. Each of the 50 CESM2-LE members is treated in turn as a surrogate "observation", and the LIM trained on the internal components of SST and SSH in that member during 1960-2022 is used to generate 50 synthetic realizations of internal variability. The internal components of SST and SSH are computed by subtracting the 50-member CESM2-LE ensemble mean at each time step and grid box. For each surrogate, the resulting distribution of synthetic 1979–2020 SST trends is compared with the corresponding distribution across the full 50-member CESM2-LE. We assess the agreement between these distributions using the equatorial Pacific zonal SST gradient index and IPWP-to-tropical-mean warming ratio index defined in Text S3. This experiment tests whether a LIM trained on a single realization can reproduce the expected spread of multidecadal SST trends arising from internal variability (Figure S6).

We further evaluate whether the LIM reproduces the spatial amplitude of SST variability in CESM2-LE by comparing spatial maps of the standard deviation of annual-mean SST anomalies and 1979–2020 SST trends generated by the LIM with those obtained directly from CESM2-LE (Figure S7). These complementary tests assess the spatial structure and amplitude of internal SST variability on interannual and multidecadal timescales, respectively. Overall, the LIM trained on each member of the CESM2-LE reproduces the amplitude of SST trend variability in the original 50-member CESM2-LE to within approximately 10–20% across most Indo-Pacific locations (Figure S7). We also evaluate the realism of CESM2 by comparing the standard deviation of internal SST trends in the OBS-LE with those in the CESM2-LE-LIM ensemble. The amplitude of 1979–2020 internal SST trend variability is generally somewhat smaller in the OBS-LE than in the CESM2-LE-based LIM realizations, with OBS-LE-to-CESM2-LIM standard-deviation ratios near 0.8 across much of the Pacific (Figure S8). However, these differences are spatially heterogeneous, with ratios of approximately 0.4 in the western equatorial Pacific and up to about 1.4 over parts of the Southern Ocean and northeastern subtropical Pacific.

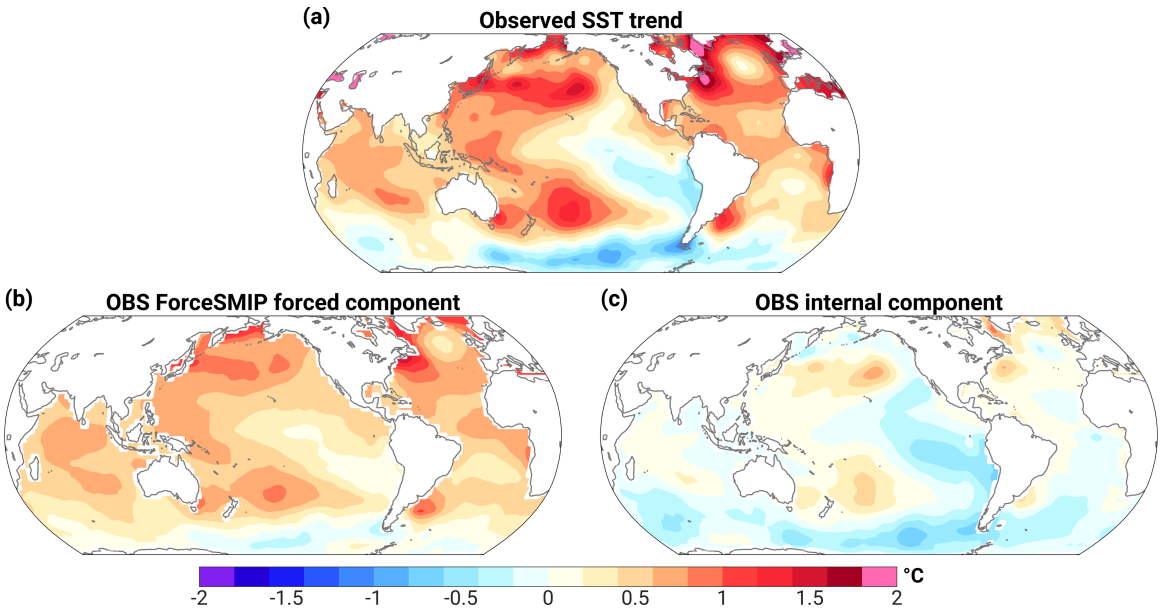


Figure S1. Decomposition of observed SST trends (°C) over 1979–2020 into forced and internal components. (a) Total SST trend from ERSSTv5, (b) externally forced component estimated as the mean across the 27 skillful ForceSMIP methods, and (c) internally generated component calculated as the difference between the ERSSTv5 total trend and the ForceSMIP estimate.

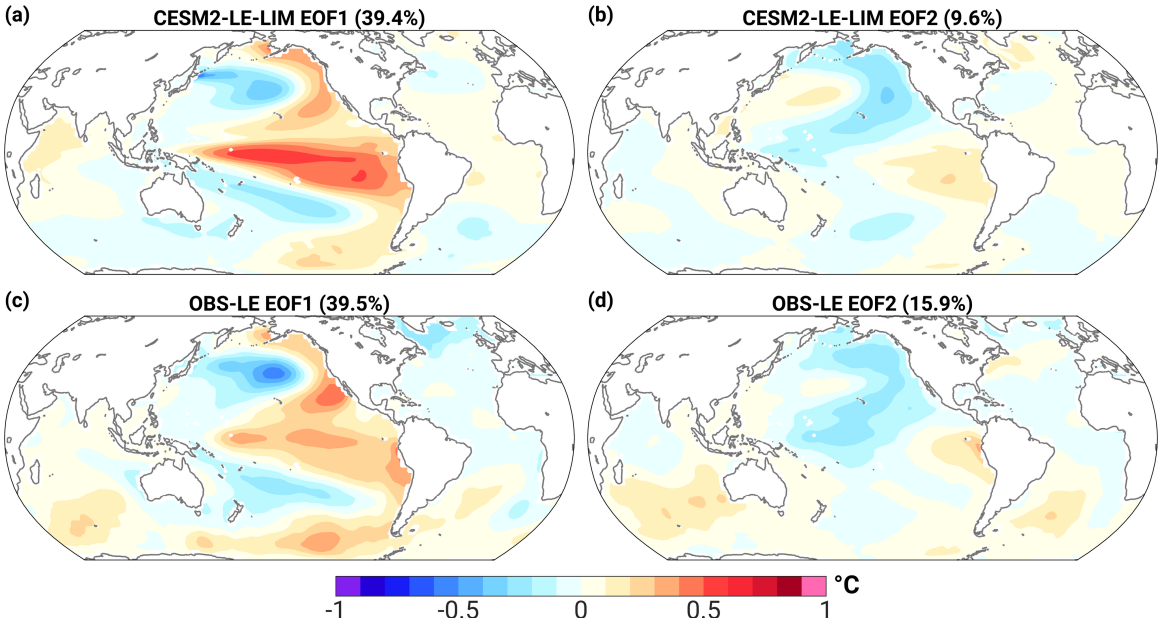


Figure S2. Leading EOF patterns of internal SST trends over 1979–2020 calculated across LIM realizations. (a, c) EOF1 and (b, d) EOF2 derived from the CESM2-LE (top) and the OBS-LE (bottom). The fraction of variance explained by each mode is shown in the corresponding panel title. The EOF analysis is performed over the pan-Pacific domain (70°S–70°N, 120°E–70°W). The displayed global patterns are obtained by regressing SST trends onto the standardized principal components (PCs).

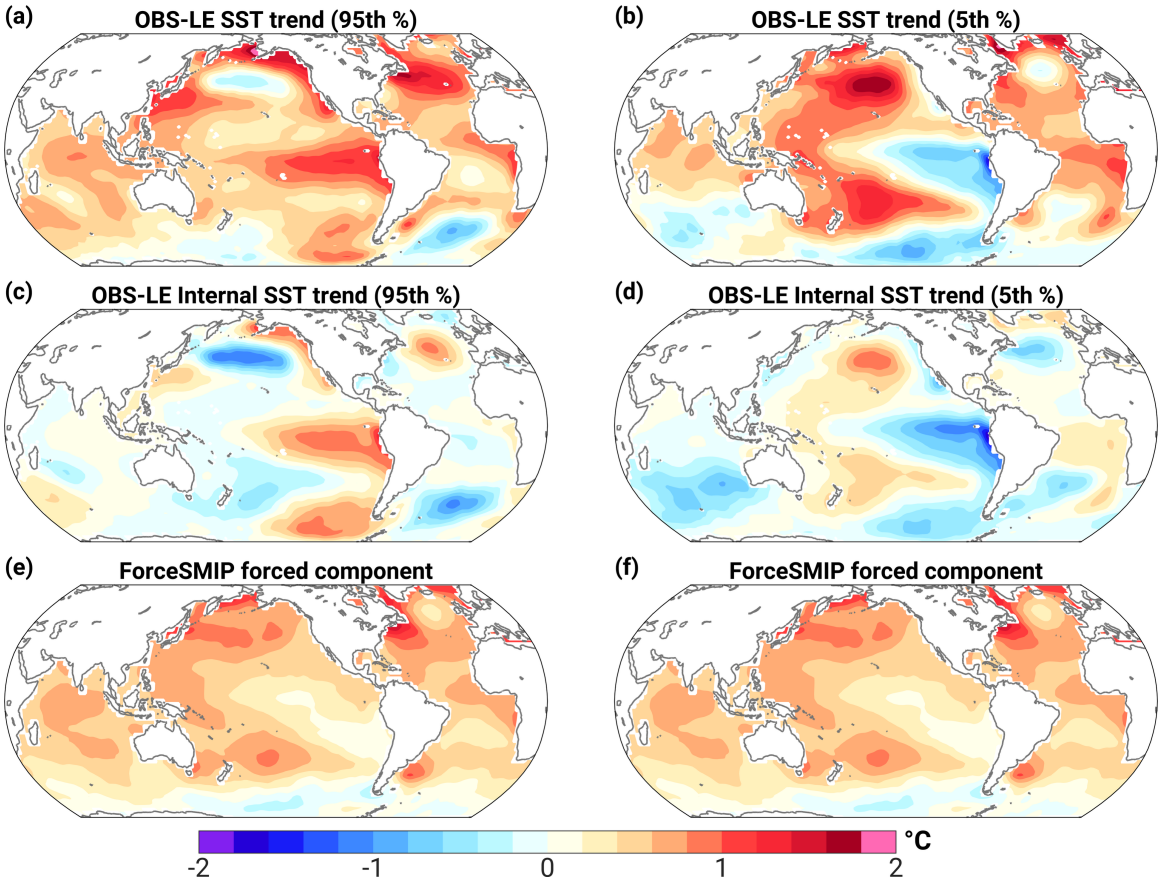


Figure S3. Plausible range of observed SST trends (°C) over 1979–2020 arising from internal variability. (a, b) Selected OBS-LE members that lie at approximately the 95th and 5th percentiles of the full (50,000 member) OBS-LE distribution based on their scores for the leading principal component of pan-Pacific internal SST trends, whose spatial pattern resembles the Interdecadal Pacific Variability pattern. (c, d) As in (a, b) but for the internal trend components, obtained by subtracting the observed ForceSMIP forced trend from the total trend. (e, f) Observed ForceSMIP forced trend.

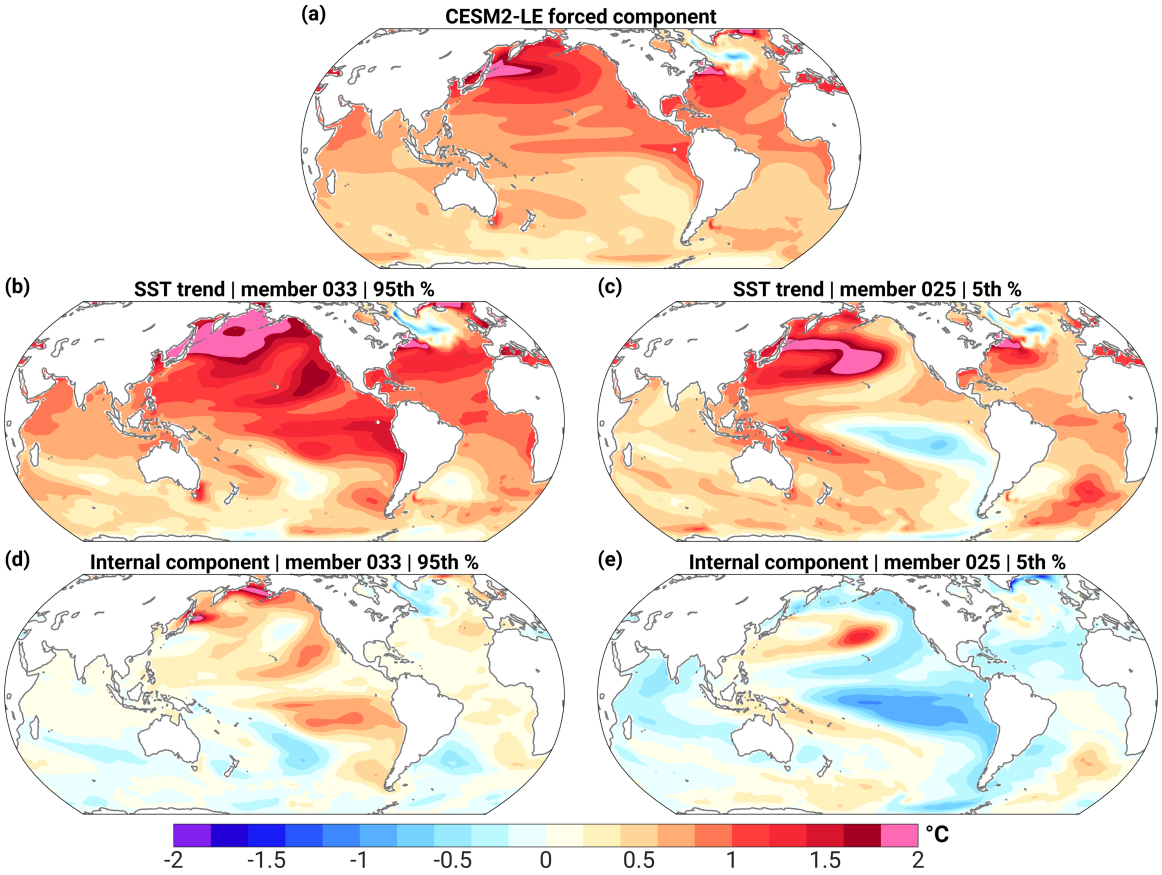


Figure S4. Decomposition of SST trends (°C) over 1979–2020 for selected CESM2-LE members into their forced and internal components. (a) The externally forced component, defined as the 50-member ensemble-mean SST trend. (b, c) Total SST trends in members 33 and 25, corresponding to the 95th- and 5th-percentiles of the leading principal component of internal SST trends, whose spatial pattern resembles Interdecadal Pacific Variability (IPV). (d, e) Internal component of SST trends in members 33 and 25, calculated by subtracting the forced component from the total trends.

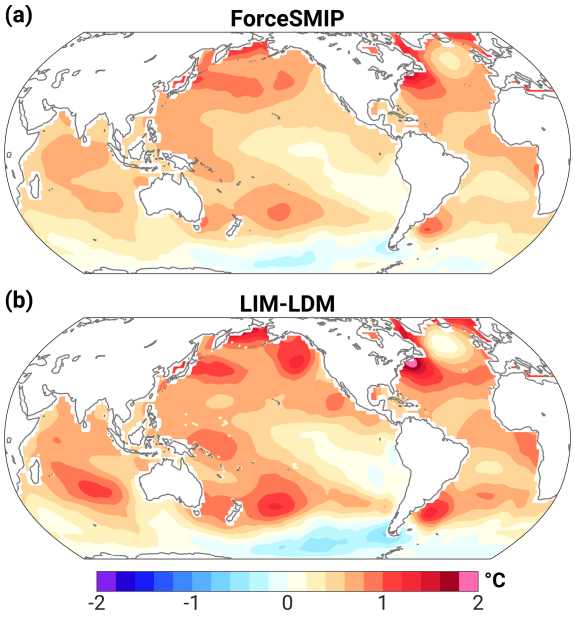


Figure S5. Forced component of observed SST trends (°C) over 1979–2020 estimated using (a) the mean across 27 skillful ForceSMIP methods and (b) the LDM of a LIM fitted to observed SST and SSH.

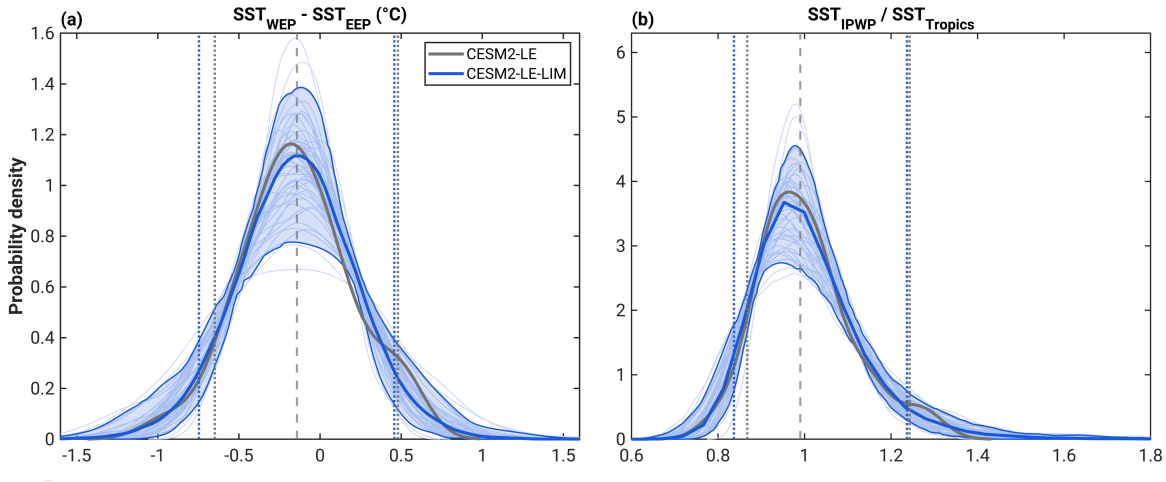


Figure S6. Perfect-model evaluation of the LIM using the CESM2-LE. Kernel density estimates of 1979–2020 trends in (a) the equatorial Pacific zonal SST-gradient index and (b) the ratio of IPWP to tropical-mean SST warming, comparing the 50-member CESM2-LE distribution (gray) with the distribution of 2,500 synthetic realizations (CESM2-LE-LIM; blue), obtained by training a LIM on each of the 50 CESM2-LE members and generating 50 realizations from each. Thin blue lines show the kernel density estimate of the 50 realizations generated from each member's LIM, and blue shading indicates the pointwise 5th–95th percentile range across these 50 member-specific density estimates. Dotted vertical lines mark the empirical 5th and 95th percentiles of the CESM2-LE (gray) and of all 2,500 CESM2-LE-LIM realizations (blue), and the dashed gray vertical line indicates the CESM2-LE ensemble-mean (forced) response. This comparison tests whether a LIM trained on a single ensemble member can reproduce the spread of each metric across the full ensemble.

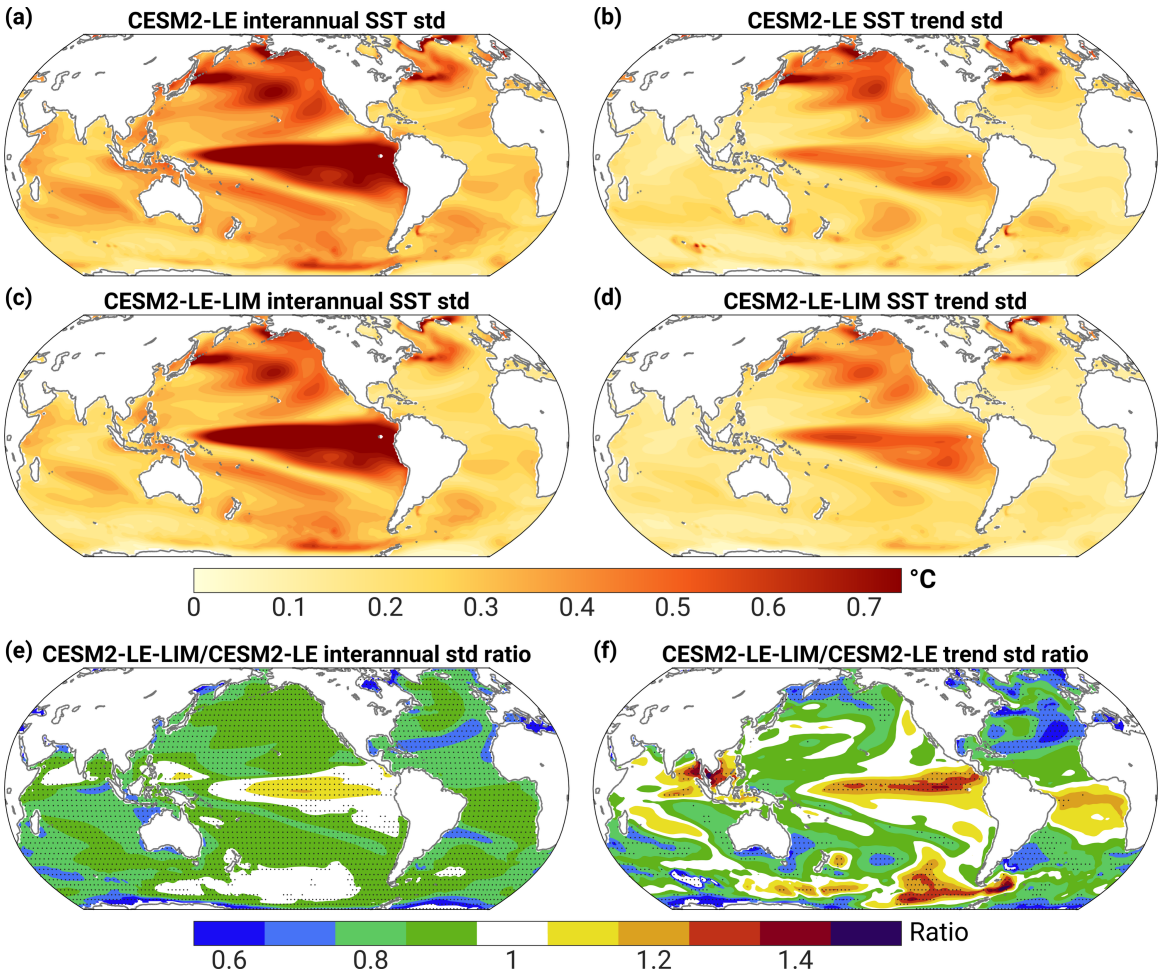


Figure S7. Standard deviation of internal SST variability from (a, b) the 50-member CESM2-LE and (c, d) CESM2-LE-LIM, and (e, f) their ratio (CESM2-LE-LIM / CESM2-LE). CESM2-LE internal variability is defined relative to the ensemble mean. CESM2-LE-LIM comprises 50 synthetic realizations from each of 50 LIMs trained separately on individual CESM2-LE members (2,500 realizations in total). Left panels (a, c, e) show interannual variability, and right panels (b, d, f) show variability in 1979–2020 SST trends. Stippling in (e, f) indicates regions where the CESM2-LE-LIM and CESM2-LE variances differ significantly at the 5% level. Significance is assessed using a two-sided F-test for interannual variability and a member-aware bootstrap test with 1,000 resamples for trend variability.

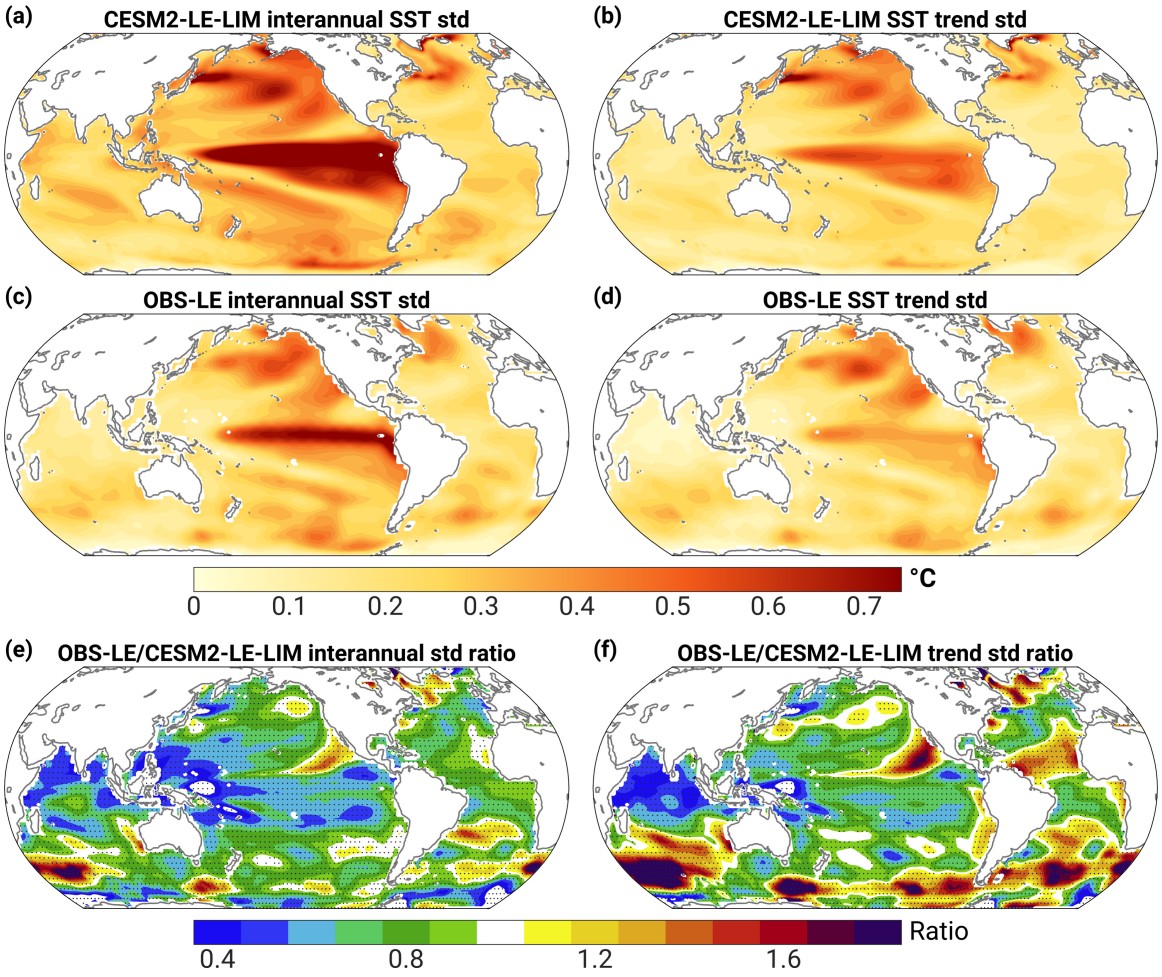


Figure S8. Comparison of the amplitude of internal SST variability between CESM2-LE-LIM and OBS-LE. SST standard deviation in (a, b) CESM2-LE-LIM, (c, d) OBS-LE and (e, f) their ratio (OBS-LE / CESM2-LE-LIM). Left panels (a, c, e) show interannual variability, and right panels (b, d, f) show variability in 1979–2020 SST trends. Stippling in (e, f) indicates regions where the OBS-LE and CESM2-LE-LIM variances differ significantly at the 5% level. Significance is assessed using a two-sided F-test for interannual variability and a member-aware bootstrap test with 1,000 resamples for trend variability.

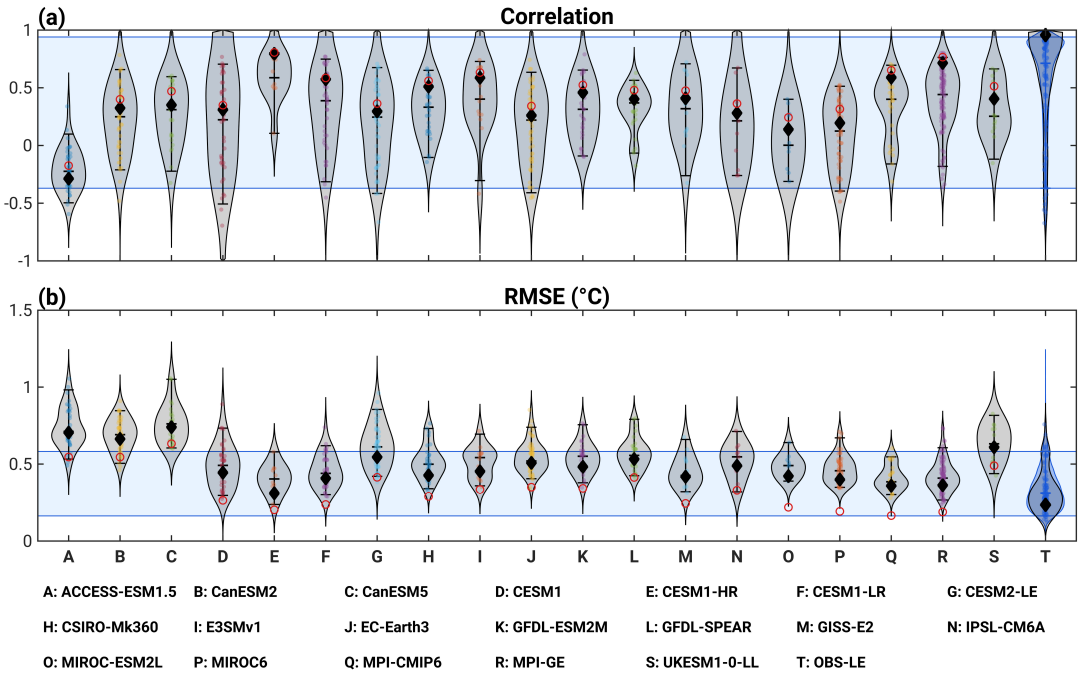


Figure S9. Distributions of (a) pattern correlation and (b) RMSE between the 1979–2020 SST trends from individual members of each model LE and ERSSTv5 over the tropical Pacific domain (30°S–30°N, 120°E–70°W; colored dots). Short horizontal black segments within each violin indicate the 5th, 50th, and 95th percentiles of the corresponding distribution. Filled black diamonds indicate the metric calculated between each model's ensemble-mean trend map and ERSSTv5, while open red circles indicate the metric calculated between each model's ensemble-mean trend map and ForceSMIP. The OBS-LE distribution is shown at the far right, with black and blue violin outlines indicating distributions calculated between ERSSTv5 and the first 100 and all 50,000 OBS-LE realizations, respectively; the black diamond indicates the metric calculated between ForceSMIP and ERSSTv5. The vertical extent of the light blue shading spans the 5th–95th percentile range calculated from the full OBS-LE.

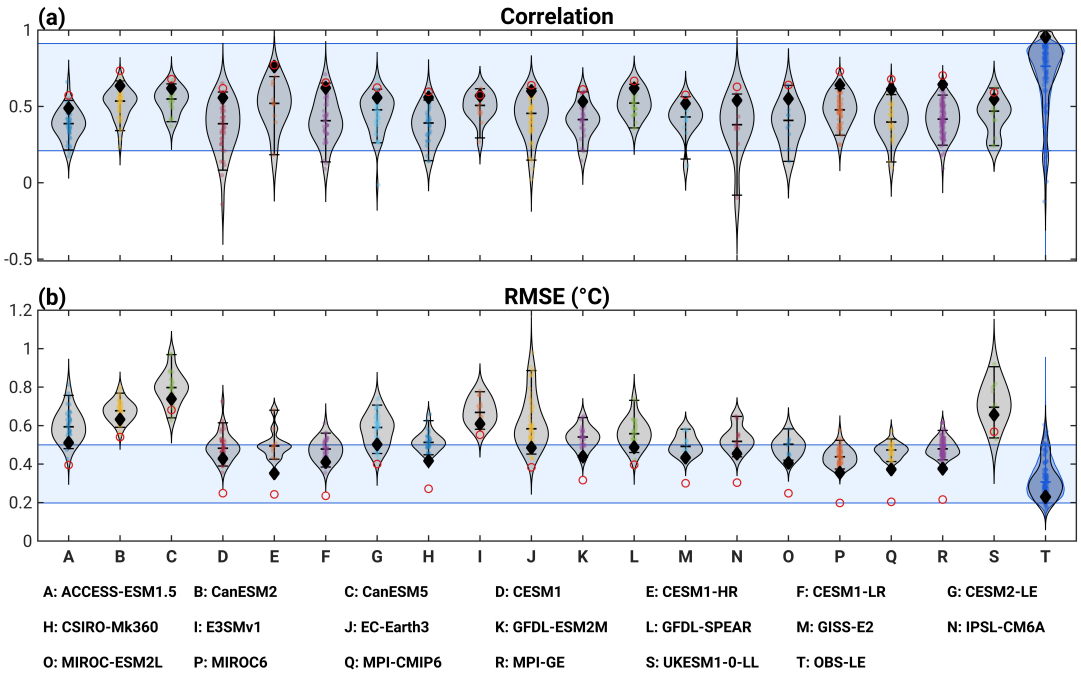


Figure S10. As in Fig. S9, but for metrics calculated over the global domain (70°S–70°N).

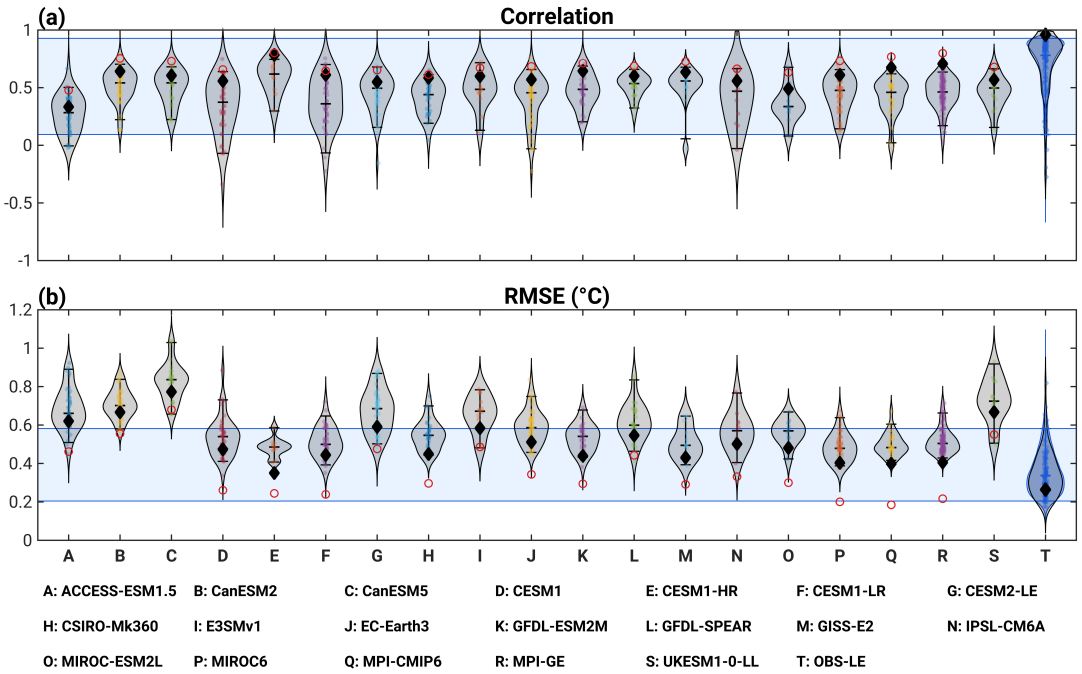


Figure S11. As in Fig. S9 but based on an OBS-LE generated using a LIM trained over the pan-Pacific domain (70°S–70°N, 120°E–70°W). Metrics are also computed over the pan-Pacific domain.

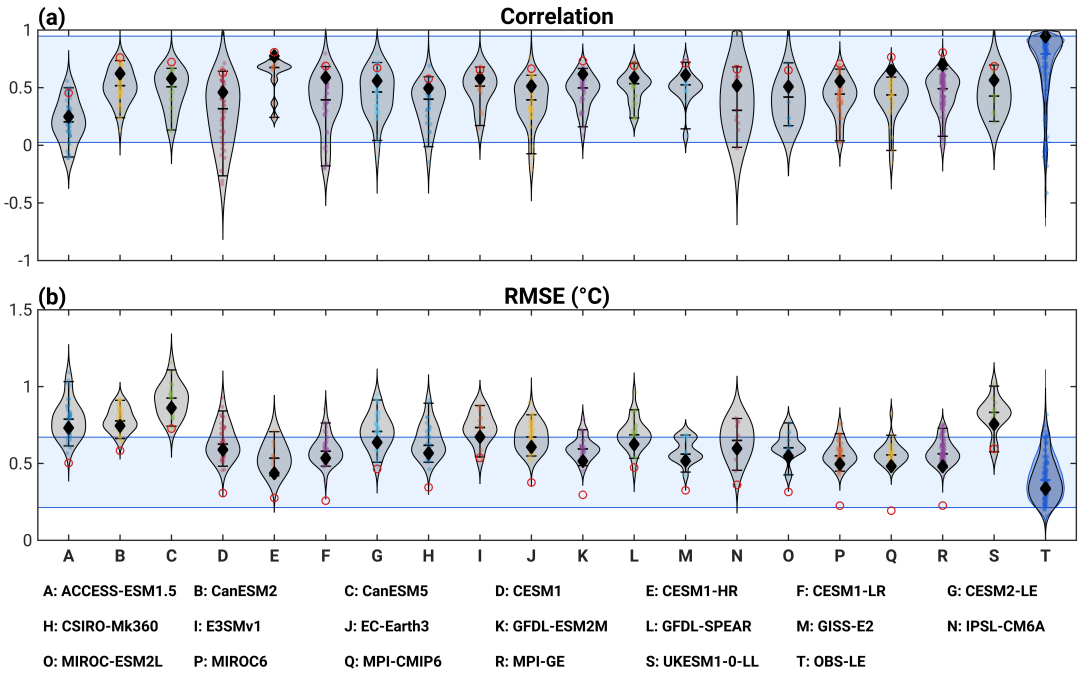


Figure S12. As in Fig. S9 but based on trends over 1980–2022 and with an OBS-LE generated using a LIM trained over 1980–2022. Metrics are computed over the pan-Pacific domain (70°S–70°N, 120°E–70°W).

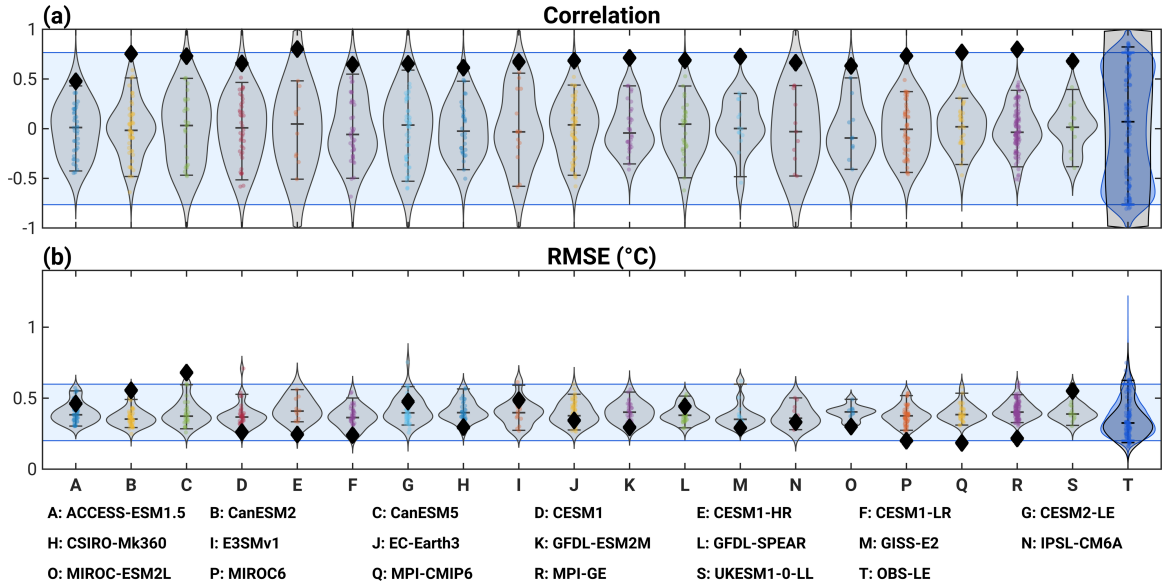


Figure S13. Distributions of (a) pattern correlation and (b) RMSE between the internal component of 1979–2020 SST trends from individual members of each model LE and from the internal component of ERSSTv5 over the pan-Pacific domain (70°S–70°N, 120°E–70°W; colored dots). Short horizontal black segments within each violin indicate the 5th, 50th, and 95th percentiles of the corresponding distribution. Filled black diamonds indicate the metric calculated between each model's ensemble-mean trend map and ForceSMIP. The OBS-LE distribution is shown at the far right, with black and blue violin outlines indicating distributions calculated between the internal component of ERSSTv5 and the internal components of the first 100 and all 50,000 OBS-LE realizations, respectively; the black diamond indicates the metric calculated between ForceSMIP and ERSSTv5. The vertical extent of the light blue shading spans the 5th–95th percentile range calculated from the full OBS-LE.

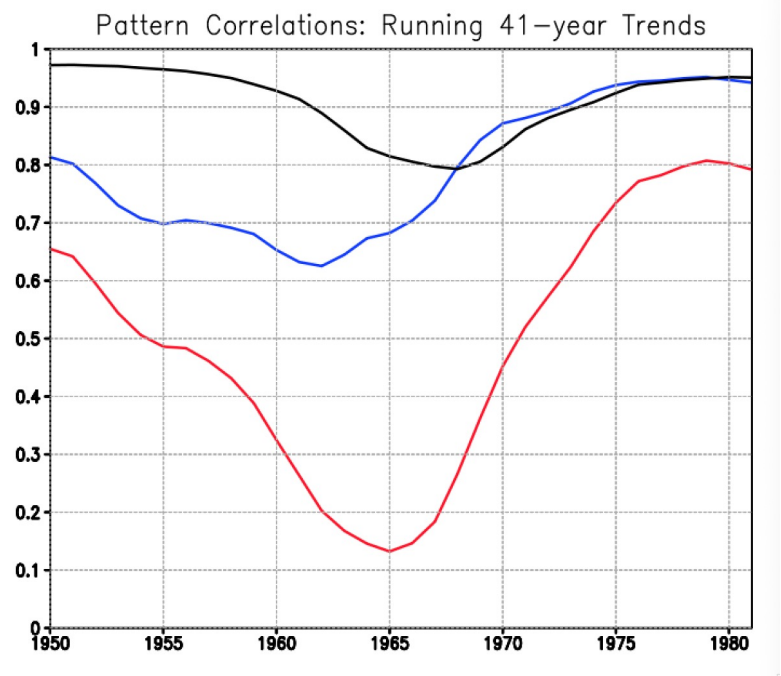


Figure S14. Pattern correlations of running 41-year SST trends over the pan-Pacific domain (70°S–70°N, 120°E–70°W) computed between the following component pairs: total ERSSTv5 and internal ERSSTv5 (black curve); total ERSSTv5 and forced ERSSTv5 (blue curve); and internal ERSSTv5 and forced ERSSTv5 (red curve). The forced component of ERSSTv5 is given by the mean across the 27 skillful ForceSMIP methods, and the internal component of ERSSTv5 is calculated as the difference between the ERSSTv5 total trend and the ForceSMIP estimate.

References

Alexander, M. A., Shin, S.-I., & Battisti, D. S. (2022). The Influence of the Trend, Basin Interactions, and Ocean Dynamics on Tropical Ocean Prediction. *Geophysical Research Letters*, *49*(3), e2021GL096120. https://doi.org/10.1029/2021GL096120

Capotondi, A., Newman, M., Xu, T., & Di Lorenzo, E. (2022a). An Optimal Precursor of Northeast Pacific Marine Heatwaves and Central Pacific El Niño Events. *Geophysical Research Letters*, *49*(5), e2021GL097350. https://doi.org/10.1029/2021GL097350

Capotondi, A., Newman, M., Xu, T., & Di Lorenzo, E. (2022b). An Optimal Precursor of Northeast Pacific Marine Heatwaves and Central Pacific El Niño Events. *Geophysical Research Letters*, *49*(5), e2021GL097350. https://doi.org/10.1029/2021GL097350

Chang, P., Fu, D., Liu, X., Castruccio, F. S., Prein, A. F., Danabasoglu, G., et al. (2026). Future extreme precipitation amplified by intensified mesoscale moisture convergence. *Nature Geoscience*, *19*(1), 33–41. https://doi.org/10.1038/s41561-025-01859-1

Hasselmann, K. (1988). PIPs and POPs: The reduction of complex dynamical systems using principal interaction and oscillation patterns. *Journal of Geophysical Research: Atmospheres*, *93*(D9), 11015–11021. https://doi.org/10.1029/JD093iD09p11015

Newman, M. (2013). An Empirical Benchmark for Decadal Forecasts of Global Surface Temperature Anomalies. https://doi.org/10.1175/JCLI-D-12-00590.1

493 Penland, C., & Matrosova, L. (1994). A Balance Condition for Stochastic Numerical
494 Models with Application to the El Niño-Southern Oscillation. Retrieved from
495 https://journals.ametsoc.org/view/journals/clim/7/9/1520-
496 0442_1994_007_1352_abcfsn_2_0_co_2.xml
497 Penland, C., & Sardeshmukh, P. D. (1995). The Optimal Growth of Tropical Sea Surface
498 Temperature Anomalies. Retrieved from
499 https://journals.ametsoc.org/view/journals/clim/8/8/1520-
500 0442_1995_008_1999_togots_2_0_co_2.xml
501 Rebert, J. P., Donguy, J. R., Eldin, G., & Wyrtki, K. (1985). Relations between sea level,
502 thermocline depth, heat content, and dynamic height in the tropical Pacific Ocean.
503 *Journal of Geophysical Research: Oceans*, *90*(C6), 11719–11725.
504 https://doi.org/10.1029/JC090iC06p11719
505 Wills, R. C. J., Dong, Y., Proistosecu, C., Armour, K. C., & Battisti, D. S. (2022).
506 Systematic Climate Model Biases in the Large-Scale Patterns of Recent Sea-
507 Surface Temperature and Sea-Level Pressure Change. *Geophysical Research*
508 *Letters*, *49*(17), e2022GL100011. https://doi.org/10.1029/2022GL100011
509 Xu, T., Newman, M., Capotondi, A., Stevenson, S., Di Lorenzo, E., & Alexander, M. A.
510 (2022). An increase in marine heatwaves without significant changes in surface
511 ocean temperature variability. *Nature Communications*, *13*(1), 7396.
512 https://doi.org/10.1038/s41467-022-34934-x
513 Zhang, X., Li, F., Jing, Z., Zhang, B., Ma, X., & Du, T. (2024). Detecting marine
514 heatwaves below the sea surface globally using dynamics-guided statistical

learning. *Communications Earth & Environment*, *5*(1), 616. https://doi.org/10.1038/s43247-024-01769-x

Zhao, Y., Newman, M., Capotondi, A., Lorenzo, E. D., & Sun, D. (2021). Removing the Effects of Tropical Dynamics from North Pacific Climate Variability. https://doi.org/10.1175/JCLI-D-21-0344.1